Synthesis of Self-Pillared Zeolite Nanosheets by Repetitive Branching

Xueyi Zhang *et al.*

Science **336**, 1684 (2012);
DOI: 10.1126/science.1221111

Science (print ISSN 0036-8075; online ISSN 1095-9203) is published weekly, except the last week in December, by the American Association for the Advancement of Science, 1200 New York Avenue NW, Washington, DC 20005.

Synthesis of Self-Pillared Zeolite Nanosheets by Repetitive Branching

Xueyi Zhang,[1] Dongxia Liu,[1] Dandan Xu,[1] Shunsuke Asahina,[2] Katie A. Cychosz,[3] Kumar Varoon Agrawal,[1] Yasser Al Wahedi,[1] Aditya Bhan,[1] Saleh Al Hashimi,[4] Osamu Terasaki,[5,6] Matthias Thommes,[3] Michael Tsapatsis[1]*

Hierarchical zeolites are a class of microporous catalysts and adsorbents that also contain mesopores, which allow for fast transport of bulky molecules and thereby enable improved performance in petrochemical and biomass processing. We used repetitive branching during one-step hydrothermal crystal growth to synthesize a new hierarchical zeolite made of orthogonally connected microporous nanosheets. The nanosheets are 2 nanometers thick and contain a network of 0.5-nanometer micropores. The house-of-cards arrangement of the nanosheets creates a permanent network of 2- to 7-nanometer mesopores, which, along with the high external surface area and reduced micropore diffusion length, account for higher reaction rates for bulky molecules relative to those of other mesoporous and conventional MFI zeolites.

Zeolites with structural features as small as the size of a unit cell (e.g., 1 to 5 nm), including those with lamellar structure (*1*–*4*), can be used as building blocks for thin films (*5*–*7*). Additionally, hierarchical adsorbents and catalysts constructed by introducing mesopores between the zeolitic domains allow access of bulkier molecules often encountered in oil and biomass processing (*8*, *9*). Methods for the preparation of mesoporous zeolites involve multifunctional structure-directing agents (SDAs) and/or postsynthesis processing, such as pillaring or desilication/dealumination (*8*, *10*–*12*). Crystal growth by repetitive branching of layers can constitute a simple, low-cost approach for bottom-up synthesis of hierarchical zeolites and pillared materials. Although branching (by twinning, rotational intergrowths, or polytypic overgrowths) has been used to design nanostructures (*13*, *14*), it has not been explored for the formation of pillared zeolites. Among several candidates of epitaxially and rotationally overgrown zeolites [e.g., MFI/MEL (*15*), EMT/FAU (*16*), ETS-4/ETS-10 (*17*), CAN/SOD (*18*), MFI (*19*), and CHA (*20*)], we focus on exploring the 90° rotational intergrowths (or twins) of the MFI framework [which contains sinusoidal 10-member ring (10-MR) channels along the *a* axis, interconnected with straight 10-MR channels along the *b* axis] motivated by the prominence of the corresponding aluminosilicate (called ZSM-5) as a catalyst in chemical processing. Such an approach uses a single, simple, and relatively inexpensive SDA. Here, we demonstrate the one-step synthesis of a hierarchical self-pillared zeolite composed of orthogonally connected single–unit cell lamellae (2 nm thick) resembling a house-of-cards construction (*21*).

We decided to explore tetrabutylphosphonium (TBP)–silica and tetrabutylammonium (TBA)–silica sols, which are known to yield MFI as well as mixtures of MFI with the related structure MEL (which contains straight 10-MR channels along the *a* axis, interconnected with straight 10-MR channels along the *b* axis) (*7*, *22*). Figure 1A shows particles obtained after 3 hours at 388 K starting from a clear sol with composition $1SiO_2$:0.3TBPOH:$10H_2O$:4EtOH (*23*) (TBPOH, tetrabutylphosphonium hydroxide; EtOH, ethyl alcohol). Figure 1B shows a high-resolution transmission electron microscopy (HRTEM) image along with the corresponding fast Fourier transform (FFT) confirming that the particles are MFI plates, thin along the *b* axis. Their thickness was determined by atomic force microscopy (AFM) (fig. S1) to be ~2 nm (i.e., a unit cell along the *b* axis), thinner than previously reported lamellae made by exfoliation (*24*). With further heat treatment, the lamellae became intergrown. After 40 hours at 388 K, the product contained crystalline particles with size varying between 100 and 200 nm (Fig. 2A). HRTEM images (Fig. 2B) showed that the particles consist of crystalline zeolite lamellae with a layer thickness of 2 nm. Remarkably, the zeolite lamellae are intergrown in a house-of-cards arrangement (i.e., with the lamellae arranged perpendicular to each other) to define pores between them. TEM images, taken after calcination in air at 823 K for 12 hours, do not reveal any change in the house-of-cards arrangement (Fig. 2C). The pores as well as the connectivity of the lamellae can also be seen by low-voltage scanning electron microscopy (SEM) from calcined samples (Fig. 2, D and E).

To further probe their internal structure, we embedded the calcined particles in polystyrene and studied thin sections by TEM. Intermittent lattice fringes, as shown in Fig. 2F, provide evidence for pores between adjacent lamellae penetrating throughout the particles. Further TEM imaging and FFT analysis (Fig. 3A) indicated that the thin dimension (~2 nm) of the lamellae is along the *b* axis of MFI and that the lamellae are longer along the *c* axis and shorter (~100 nm) along the *a* axis. Additional synthesis and characterization (figs. S2 and S3) show that the self-pillared zeolite can be prepared in a range of conditions that allow manipulation of composition and particle size (supplementary text).

Two plausible models for the local structure of the intergrown lamellae are shown in the

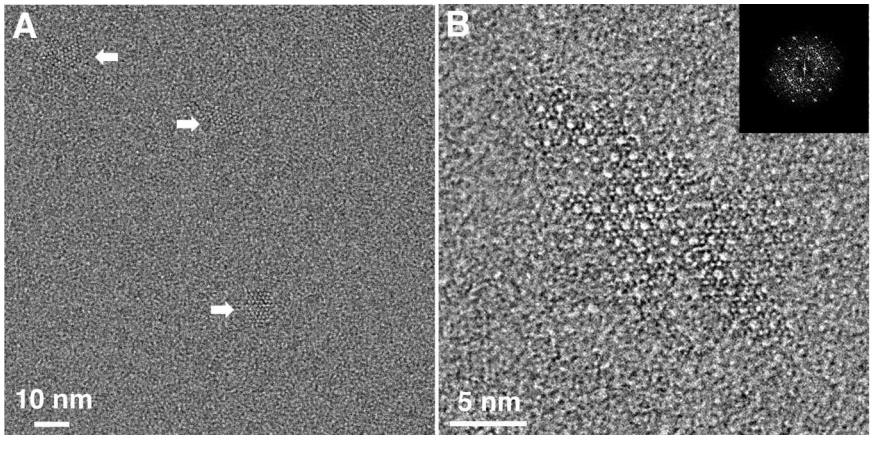

Fig. 1. (**A**) TEM image of zeolite nanoparticles obtained after 3 hours at 388 K. (**B**) High-resolution TEM image of a representative zeolite particle obtained after 7 hours at 388 K. Both samples were first aged at 353 K for 2 days. The inset in (B) is the fast Fourier transform (FFT) of the high-resolution TEM image.

[1]Department of Chemical Engineering and Materials Science, University of Minnesota, Minneapolis, MN 55455, USA. [2]SM Application Group, JEOL Ltd., Akisima, Tokyo 196-8558, Japan. [3]Quantachrome Instruments, 1900 Corporate Drive, Boynton Beach, FL 33426, USA. [4]Chemical Engineering Program, Petroleum Institute, Abu Dhabi, United Arab Emirates. [5]Graduate School of Energy, Environment, Water and Sustainability (EEWS), World Class University Program, Korea Advanced Institute of Science and Technology, 291 Daehak-ro (373-1 Guseong-dong), Yuseong-gu, Daejeon 305-701, Republic of Korea. [6]Department of Materials and Environmental Chemistry and Bezelii Center EXSELENT on Porous Materials, Stockholm University, SE-106 91 Stockholm, Sweden.

*To whom correspondence should be addressed. E-mail: tsapatsis@umn.edu

insets of Fig. 3B. According to these idealized fragment models, single–unit cell MFI lamellae (with thickness of one unit cell along the *b* axis of the MFI structure) are intergrown with their 90° twins or rotational intergrowths having a common *c* axis. In one of the idealized models, we hypothesize that the twins are connected through a needle of MEL (1 × 1 unit cell across and elongated along the *c* axis). The MEL connection runs through the entire interface of the MFI twins, ensuring full connectivity. There are 12 different ways to make the idealized connection; one of these is shown in the lower inset of Fig. 3B (see fig. S4 for the others). In the actual material, looser connections are possible (as depicted schematically in fig. S5, A to C), with partial overlay of the MFI lamellae. An idealized fragment with no connection between the MFI lamellae is also shown in the upper inset of Fig. 3B. TEM images from particles at an early stage of intergrowth (fig. S5, D and E) provide evidence for the presence of single–unit cell outgrowths emerging from the MFI plates. MEL/MFI intergrowths when using TBA and TBP ions have been reported before (*15*, *25*), and twining or rotational intergrowths are well known in MFI crystals. However, they were not associated with single–unit cell lamellae formation or with repetitive branching to create a hierarchical zeolite. The tetrabutyl SDA, which is stable at crystal growth conditions and is incorporated intact in the framework (fig. S6), appears to be an important contributor to the anisotropic growth giving rise to the single–unit cell lamellae. In the range of MFI and MEL reflections, the simulated powder x-ray diffraction (XRD) pattern of both fragment models, obtained using UDSKIP (*23*), are in good agreement with the experimental data (Fig. 3B). At lower angles, the simulation shows broad reflections (similar for both fragments) due to the small dimensions of the fragment model. As expected, these reflections are absent from the experimental diffraction pattern of the 100- to 200-nm crystals because even though they consist of numerous interconnected fragments, they preserve their crystallographic alignment (long-range order) due to the ordered branching growth mechanism. Because the new material could be an MFI/MEL intergrowth, we refer to it as self-pillared pentasil (SPP) zeolite, although it consists mostly of MFI with MEL being present, if at all, at the branching points.

We carried out the exfoliation procedure developed by Maheshwari *et al*. (*26*) on the as-synthesized material. As shown in fig. S7, it is possible to obtain individual lamellae. The high-resolution TEM image from one isolated lamella (fig. S7B) further confirms that the thickness of the lamellae is 2 nm. The exfoliated lamellar zeolites can be potentially used as building units for selective membranes according to the procedure recently reported in (*24*).

To explore the catalytic properties of SPP zeolites, we incorporated Al in the framework (fig. S8) at two different ratios of Si/Al: 253 and 75, both of which required the addition of NaOH (*23*). Synthesis in the presence of sodium and aluminum did not prevent branching and self-pillaring, as clearly seen by TEM imaging (fig. S8, A and B). Argon adsorption isotherms at 87.3 K and pore size analysis are given in figs. S10 to S12. The cumulative pore volume plots calculated from nonlocal density functional theory (NLDFT) (*27*) over the complete pore size range are shown in Fig. 3C and indicate the presence

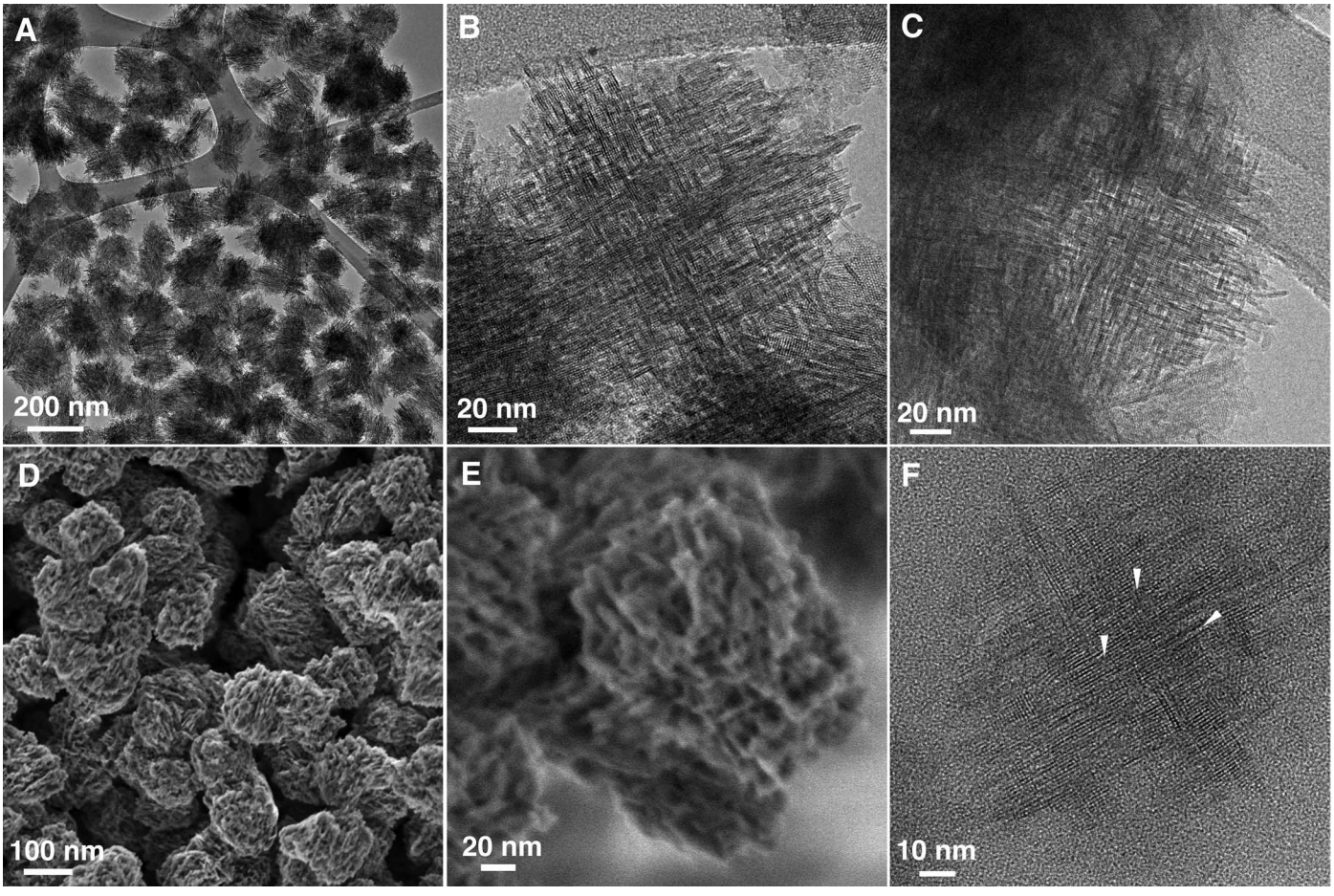

Fig. 2. Structure and morphology of the pure-silica self-pillared pentasil (SPP) zeolite particles after 40 hours of hydrothermal synthesis at 388 K. (**A** and **B**) Low-magnification (A) and high-magnification (B) TEM images of the particles before calcination, showing the morphology and the mesopores formed within the intersecting zeolitic lamellae. (**C**) TEM image of the particles after calcination, showing the retained mesoporosity. (**D** and **E**) Low-voltage, high-resolution SEM images of the calcined particles at two different magnifications, showing the mesopores and lamellar connectivity. (**F**) High-resolution TEM image of a thin section of the calcined zeolite embedded in polystyrene. Intermittent lattice fringes (arrows) suggest that mesopores exist throughout the particle.

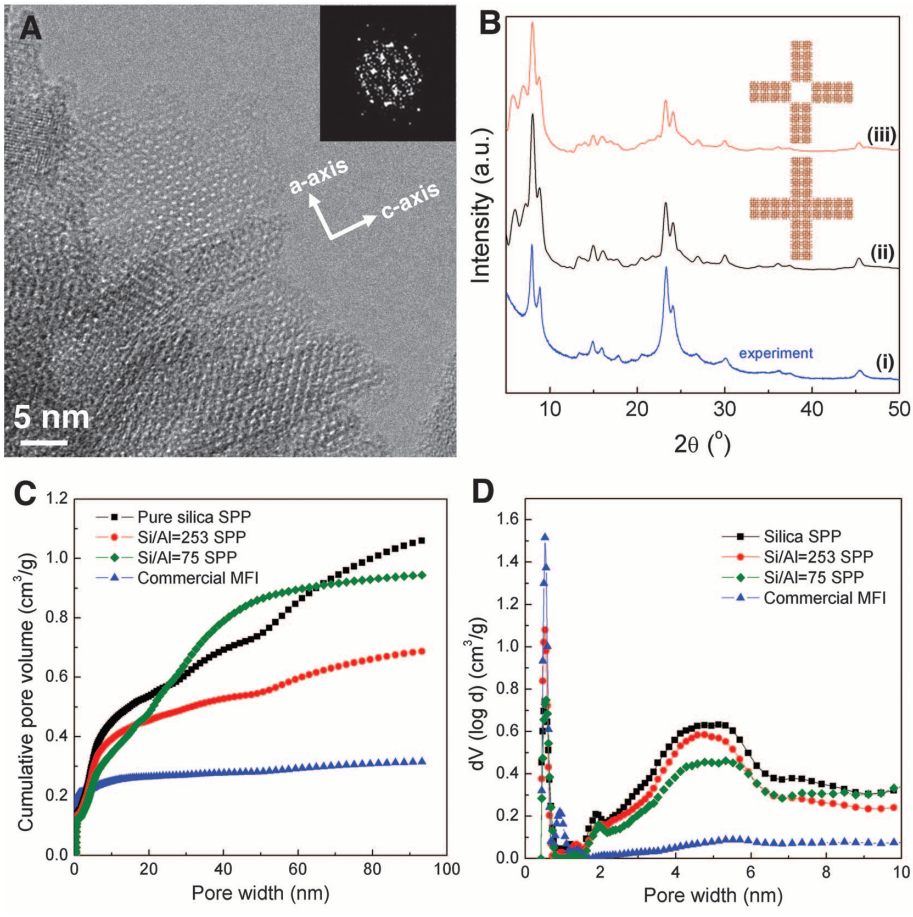

Fig. 3. (**A**) High-resolution TEM image of a SPP lamella viewed across its thin dimension; the FFT from the lamella is consistent with the [010]-zone axis of zeolite MFI. (**B**) Experimental (i) and simulated (ii and iii) powder XRD patterns of the pure-silica SPP zeolite. Insets show the intergrowth models from which the simulated XRD patterns were obtained; the model for trace ii is the idealized MFI/MEL model, that for trace iii is the idealized model with MEL removed, and the dimension of the model along the common *c* axis is 10 unit cells. (**C** and **D**) Argon (87.3 K) NLDFT cumulative pore volume plots over the entire pore width range (C) and pore size distributions up to 10 nm (D) for silica (squares), aluminosilicate SPP zeolite (circles, Si/Al = 253; diamonds, Si/Al = 75), and commercial MFI (triangles).

of micro- and mesoporosity in the SPP samples. The pore size distributions plotted up to 10 nm (Fig. 3D) indicate micropores centered around 0.522 nm, typical of MFI and MEL, and a broad distribution of mesopores (from ~2 to 7 nm) for both the silica and aluminosilicate SPP, in good agreement with the TEM and SEM images.

The catalytic properties of SPP were compared with those of pillared MFI (*3*), three-dimensionally ordered mesoporous-imprinted (3DOm-i) MFI, and three conventional MFI catalysts with different crystal size (17, 1.4, and 0.2 μm) (*23*). The Brønsted acid site concentrations of all zeolites, including that of the aluminosilicate SPP, were determined by chemical titration methods (*28*) and were found to agree well with those expected from the Si/Al ratio from elemental analysis (table S1). The fraction of acid sites present at the external surface was determined for each catalyst by means of a titrant molecule, 2,6-di-*tert*-butylpyridine (DTBP), that cannot enter the zeolite pores. The results were in good agreement with the values expected from the external surface areas of the corresponding catalysts (*9*) (table S1). Specifically, 30% and 45% of the acid sites in pillared MFI and SPP, respectively, are sites that are accessible by a molecule that cannot enter the micropores; for a micrometer-sized crystal, this fraction is ~2%. As a result of the increase in number of accessible acid sites, the pseudo–first-order rate constant for the liquid-phase alkylation of mesitylene (a molecule that is effectively excluded from the zeolite micropores) by benzyl alcohol was found to vary by more than two orders of magnitude (fig. S14 and table S2, column 2). However, when normalized per external acid site, the rate constant was found to be nearly invariant across all samples tested (Fig. 4A and table S2, column 3); this shows that the reactivity of external acid sites is similar among all samples tested, despite the different morphologies and synthesis conditions.

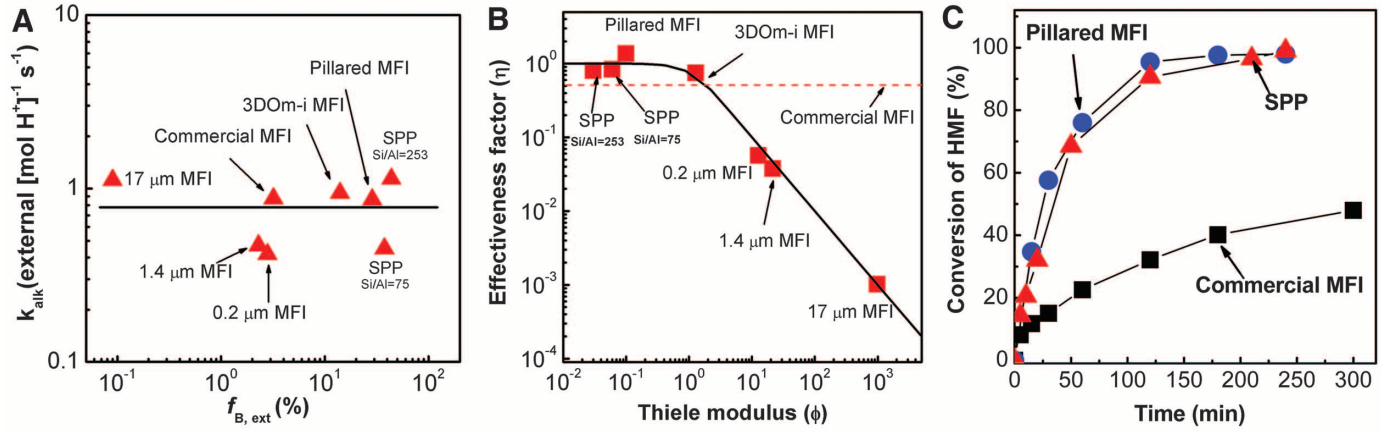

Fig. 4. Comparison of catalytic performance of SPP zeolite with pillared, 3DOm-i, and commercial and conventional (0.2, 1.4, and 17 μm) MFI. (**A**) Pseudo–first-order rate constant per external Brønsted acid site for mesitylene alkylation by benzyl alcohol. (**B**) Effectiveness factor versus Thiele modulus plot (solid line) and experimental data. The effectiveness factor of commercial MFI is indicated by the dashed line because the particle size of the commercial zeolite as determined by SEM is broad (0.1 to 1 μm) and therefore, its Thiele modulus cannot be determined. (**C**) Plots of HMF-to-OBMF conversion versus time for pillared MFI (circles), SPP zeolite (triangles), and commercial MFI (squares).

MFI lamellae are unique among the available aluminosilicate zeolite lamellae because they have pores that run across the lamella thickness (*3*). The nanometer-scale diffusion lengths of pillared MFI and SPP allow for fast transport even for molecules with small micropore diffusivity. In this respect, pillared MFI and SPP are valuable model materials for the quantitative assessment of diffusion limitations and intrinsic kinetics. The self-etherification of benzyl alcohol in the presence of DTBP (used in order to deactivate the external sites) was considered as an example. The plot of the effectiveness factor versus the Thiele modulus shows excellent agreement with the experimental data (*23*, *29*), from which it can be concluded that Brønsted acid sites in the micropores of SPP and pillared MFI have reactivity similar to those in conventional and nanocrystalline MFI, and that the observed differences in apparent reaction rates can be fully accounted for by diffusion limitations. A comparison of effectiveness factors with that of a commercially available ZSM-5 catalyst (dashed line in Fig. 4B) reveals that 3DOm-i, pillared MFI, and SPP catalysts exhibit higher apparent reaction rates. Improved behavior of pillared MFI and SPP was also established in other reactions. For example, etherification of 5-hydroxymethyl-2-furaldehyde (HMF) to 5,5′-oxy(bismethylene)-2-furaldehyde (OBMF) proceeds to completion, whereas commercial ZSM-5 suffers from deactivation (Fig. 4C). Because OBMF is a desirable biobased intermediate (*30*), this finding underscores the potential of single–unit cell layers in applications beyond petrochemical processing.

Branching of zeolite nanometer-sized lamellae, through repetitive twinning or other intergrowth processes, is a new low-cost approach toward hierarchical materials with interconnected micropores and mesopores. It is in principle applicable to all zeolite structures that can (i) be grown anisotropically as thin layers and (ii) can support branching at certain acute angles (supplementary text and fig. S16).

References and Notes

1. A. Corma, V. Fornes, S. B. Pergher, T. L. M. Maesen, J. G. Buglass, *Nature* **396**, 353 (1998).
2. Y. X. Wang, H. Gies, B. Marler, U. Muller, *Chem. Mater.* **17**, 43 (2005).
3. K. Na *et al.*, *J. Am. Chem. Soc.* **132**, 4169 (2010).
4. W. J. Roth, D. L. Dorset, *Micropor. Mesopor. Mater.* **142**, 32 (2011).
5. M. A. Snyder, M. Tsapatsis, *Angew. Chem. Int. Ed.* **46**, 7560 (2007).
6. M. Tsapatsis, *Science* **334**, 767 (2011).
7. Z. J. Li, C. M. Lew, S. Li, D. I. Medina, Y. S. Yan, *J. Phys. Chem. B* **109**, 8652 (2005).
8. J. Pérez-Ramírez, C. H. Christensen, K. Egeblad, C. H. Christensen, J. C. Groen, *Chem. Soc. Rev.* **37**, 2530 (2008).
9. D. Liu, A. Bhan, M. Tsapatsis, S. Al Hashimi, *ACS Catal.* **1**, 7 (2011).
10. J. Wang, W. Yue, W. Zhou, M.-O. Coppens, *Micropor. Mesopor. Mater.* **120**, 19 (2009).
11. D. P. Serrano *et al.*, *Catal. Today* **168**, 86 (2011).
12. K. Na *et al.*, *Science* **333**, 328 (2011).
13. L. Manna, D. J. Milliron, A. Meisel, E. C. Scher, A. P. Alivisatos, *Nat. Mater.* **2**, 382 (2003).
14. Y.- Jun, H.-W. Chung, J.- Jang, J. Cheon, *J. Mater. Chem.* **21**, 10283 (2011).
15. T. Ohsuna, O. Terasaki, Y. Nakagawa, S. I. Zones, K. Hiraga, *J. Phys. Chem. B* **101**, 9881 (1997).
16. M. M. J. Treacy, D. E. W. Vaughan, K. G. Strohmaier, J. M. Newsam, *Proc. R. Soc. A* **452**, 813 (1996).
17. H. K. Jeong, J. Krohn, K. Sujaoti, M. Tsapatsis, *J. Am. Chem. Soc.* **124**, 12966 (2002).
18. T. Okubo *et al.*, *Angew. Chem. Int. Ed.* **40**, 1069 (2001).
19. L. Karwacki *et al.*, *Nat. Mater.* **8**, 959 (2009).
20. G. R. Millward, S. Ramdas, J. M. Thomas, *Proc. R. Soc. A* **399**, 57 (1985).
21. K. Möller, T. Bein, *Science* **333**, 297 (2011).
22. L. Y. Hou, L. B. Sand, in *Proceedings of the Sixth International Zeolite Conference*, D. Olson, A. Bisio, Eds. (Butterworths, Guildford, UK, 1983), pp. 887–893.
23. See supplementary materials on *Science* Online.
24. K. Varoon *et al.*, *Science* **334**, 72 (2011).
25. A. Tuel, Y. B. Taarit, *Micropor. Mater.* **2**, 501 (1994).
26. S. Maheshwari *et al.*, *J. Am. Chem. Soc.* **130**, 1507 (2008).
27. P. I. Ravikovitch, A. V. Neimark, *Colloids Surf. A* **187–188**, 11 (2001).
28. P. Cheung, A. Bhan, G. J. Sunley, E. Iglesia, *Angew. Chem. Int. Ed.* **45**, 1617 (2006).
29. R. Aris, in *Elementary Chemical Reactor Analysis* (Dover, Boston, 1989), chap. 6.
30. O. Casanova, S. Iborra, A. Corma, *J. Catal.* **275**, 236 (2010).

Acknowledgments: We acknowledge support, for all aspects of SPP zeolite, from the Catalysis Center for Energy Innovation (award DESC00001004), an Energy Frontier Research Center funded by the U.S. Department of Energy, Office of Science, Office of Basic Energy Sciences. Partial support for synthesizing conventional, 3DOm-i, and pillared zeolites and their catalytic testing was provided by ADMIRE (Abu Dhabi–Minnesota Institute for Research Excellence), NSF Emerging Frontiers in Research and Innovation grant 0937706, and the Initiative for Renewable Energy and the Environment, a program of the University of Minnesota's Institute on the Environment. Portions of this work were conducted at the University of Minnesota Characterization Facility, which receives partial support from NSF through the NNIN program. Computing resources were provided by the Minnesota Supercomputing Institute. Supported by a University of Minnesota Graduate School doctoral dissertation fellowship (X.Z.) and by ADGAS and GASCO (Y.A.W.). We thank T. Ohsuna for helpful suggestions and S. Hwang for obtaining solid-state NMR spectra. M.T. has an equity interest in, and serves as the Chief Scientific Officer for, Argilex, a company that may commercially benefit from the results of this research. M.T., X.Z., and the University of Minnesota have financial interests arising from a right to receive royalty income under the terms of a license agreement with Argilex. These relationships have been reviewed and managed by the University of Minnesota in accordance with its conflict of interest policies. A U.S. patent application by M.T. and X.Z. was filed on 3 November 2011 (Application No. 13/288,595).

Supplementary Materials

www.sciencemag.org/cgi/content/full/336/6089/1684/DC1
Materials and Methods
Supplementary Text
Figs. S1 to S16
Tables S1 and S2
References (*31*–*40*)

27 December 2011; accepted 8 May 2012
10.1126/science.1221111

Seemingly Anomalous Angular Distributions in H + D_2 Reactive Scattering

Justin Jankunas,[1] Richard N. Zare,[1]* Foudhil Bouakline,[2] Stuart C. Althorpe,[3] Diego Herráez-Aguilar,[4] F. Javier Aoiz[4]

When a hydrogen (H) atom approaches a deuterium (D_2) molecule, the minimum-energy path is for the three nuclei to line up. Consequently, nearly collinear collisions cause HD reaction products to be backscattered with low rotational excitation, whereas more glancing collisions yield sideways-scattered HD products with higher rotational excitation. Here we report that measured cross sections for the H + D_2 → HD(v' = 4, j') + D reaction at a collision energy of 1.97 electron volts contradict this behavior. The anomalous angular distributions match closely fully quantum mechanical calculations, and for the most part quasiclassical trajectory calculations. As the energy available in product recoil is reduced, a rotational barrier to reaction cuts off contributions from glancing collisions, causing high-j' HD products to become backward scattered.

It is tempting and even at times quite insightful to describe the dynamics of chemical reactions in simple terms of classical billiard-ball collisions. In this picture, the impact parameter is defined as the distance of closest approach of the centers of the two billiard balls if they could travel without interaction in straight lines. Consider what happens when a billiard ball strikes another at rest. For a head-on collision, corresponding to zero impact parameter, the incoming billiard ball recoils backward in the center-of-mass frame. For a glancing collision between the two billiard balls, corresponding to a larger impact parameter, the incoming ball is scattered more sideways with respect to its initial direction. Next, consider the more complicated case of an atom A colliding with a diatomic molecule BC at rest to form by direct reaction the products AB and C. Furthermore, let us suppose that the

[1]Department of Chemistry, Stanford University, Stanford, CA 94305–5080, USA. [2]Institut für Chemie, Universität Potsdam, Karl-Liebknecht-Strasse 24-25, 14476 Potsdam-Golm, Germany. [3]Department of Chemistry, University of Cambridge, Lensfield Road, Cambridge CB2 1EW, UK. [4]Departamento de Química Física, Facultad de Química, Universidad Complutense, 28040 Madrid, Spain.

*To whom correspondence should be addressed. E-mail: zare@stanford.edu